Effect of Reynolds Number on Detached Eddy Simulation of Hypersonic Base Flow

Krishnendu Sinha*
Indian Institute of Technology Bombay, India 400076

Abstract

Flow field around a hypersonic re-entry configuration is computed using the Detached eddy simulation methodology at two different Reynolds numbers. The lower Reynolds number condition corresponds to the 35 km altitude trajectory point of the Fire II vehicle. The near wake is found to be transitional these free-stream conditions, and the computations highlight the limitations of DES in low Re flows. The higher Re computations are performed at a free-stream density that is higher than the earlier value by a factor of 10. The time-averaged flow solutions are compared to study the effect of Reynolds number on the DES methodology and predictions. The analysis brings out interesting parallels between the two flowfields. The differences between DES and RANS predictions at the two Reynolds number are also discussed.

Introduction

Aerodynamic and thermal loads on the afterbody of re-entry vehicles are important in vehicle drag, heat shield design, payload placement and stability. There is considerable uncertainty in predicting the afterbody and wake flow field, which is often compensated by large factor of safety in the heat shield design.[1] The Reynolds number in the later part of re-entry can be high enough for transition to turbulence in the wake. Turbulent mixing alters the structure of the wake and significantly increases the heat transfer rate to the afterbody. Therefore, validation of current and advanced simulation methods for turbulent separated flows under these high Mach number conditions is important.

RANS has been traditionally used for computing time-averaged solutions of turbulent flowfields. However, RANS turbulence can yield significant error in regions of large-scale separation. For example, RANS solutions are too dissipative in bluff bodies wakes, resulting in too small a recirculation bubble and underprediction of base pressure. By comparison, detached eddy simulation improves predictions in massively separated flows.[2] Re-entry configurations with large scale separation behind them are ideal cases for which DES can be applied. Sinha *et al.*[3] and Barhardt *et al.*[4] present results for the Fire II, a proposed Titan entry vehicle and the Reentry F configurations. As mentioned in Ref. 3 hypersonic simulations are more challenging than lower Mach number cases due to the strong gradients in the shock and expansion waves. Also, heat transfer prediction is of interest, in addition to base pressure and size of recirculation bubble.

The 35 km altitude Fire II conditions used in Ref. 3 correspond to the lowest altitude, and therefore highest Reynolds number, for which in-flight measurements are available. However, the flow in the near wake is at best transitional. DES has certain limitations at these low Reynolds number conditions. Grid refinement in the DES focus region is found to lower eddy viscosity to vanishing levels. In the absence of significant turbulent eddy viscosity, control of the numerical dissipation becomes the key to obtaining grid-converged results. In the limit of vanishing numerical dissipation, a detached eddy simulation with insignificant eddy viscosity will become a direct simulation where all relevant length and time scales of turbulence are computed.

The sensitivity of DES to focus region grid spacing is expected to be lower at higher Re, where the turbulent eddy viscosity is significantly larger than the molecular and numerical viscosities. In this paper, we do a controlled experiment by increasing the freestream gas density, and therefore Re, by a factor of 10. while keeping the other freestream variables identical to the flight conditions. The resulting flow field is compared to the earlier simulation[3] at the flight conditions to study the behavior of the DES methodology with varying Re at a constant Mach number.

The remainder of the paper is organized as follows. The vehicle geometry and test conditions are given in the next section. This is followed by a description of the solution methodology and design of computational

* Assistant Professor, Department of Aerospace Engineering, Indian Institute of Technology Bombay. Member AIAA.

grids. The instantaneous and time-averaged results obtained using DES are then presented. Finally, the effect of Reynolds on the flow pattern and aerodynamic predictions are discussed.

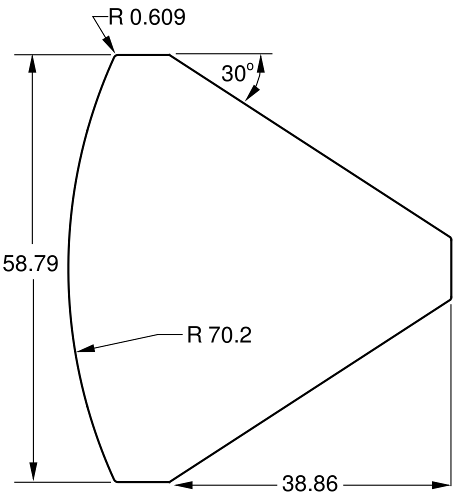

Figure 1. Fire II re-entry configuration used in the current simulations. All dimensions are in cm.

Vehicle geometry and flow conditions

The vehicle geometry used in the current work, shown in Fig. 1, corresponds to the Fire II re-entry configuration in the later part of its trajectory after the first two heat-shields are jettisoned. The freestream conditions correspond to the 35 km altitute condition.[5] The density, temperature and velocity at this trajectory point are 0.0082 kg/m^3, 237 K and 5 km/s (Mach 16), respectively. The surface temperature is taken to be 553.3 K based on the in-flight calorimeter measurements.[5] The angle of attack is assumed to be zero, because the angle-of-attack variations in flight had very little effect on the measured afterbody data. The Reynolds number based on free stream conditions and body diameter is 1.76×10^6. Blunt body separation shear layer and inner wake transition correlations are presented by Lees,[6] where the transition Reynolds number is given as a function of the local Mach number outside the wake. Based on these correlations and data from preliminary simulations, the wake is expected to transition upstream of the neck.

Simulation Methodology

The flow field around the re-entry configuration is simulated by solving the three-dimensional Favre-averaged Navier-Stokes equations. The numerical method uses a modified (low dissipation) form of Steger-Warming flux vector splitting[7] for evaluating the convective fluxes. Central differencing is used for the viscous fluxes and source terms. The turbulence model equation is fully coupled with the mean flow equations and the code is implemented in parallel using the Message Passing Interface.[8] The code has been systematically validated for flat plate boundary layers and blunt body flows. A axi-symmetric version of the code has also been applied to shock-shock interaction flows.[9]

The defining length scale of the SA model is the distance to the closest wall d. To make the model operate in DES mode one simply substitutes a new length scale d_{des} in place of d. d_{des} is defined as:

$$d_{des} = \min(d, C_{des}\Delta)$$

where Δ is the largest dimension of the local grid cell. In the near-wall region, $d_{des} = d$ and the model works in the RANS mode. Away from solid walls, $C_{des}\Delta < d$ and the destruction term is balanced by production. This results in $\nu_t \propto S\Delta^2$ which is similar to the Smagorinski model for sub-grid scales in a large eddy simulation (LES). Thus, the method switches to LES mode away from solid walls. Here, C_{des} is an adjustable parameter which was calibrated by Shur *et al.*[10] in simulations of isotropic turbulence and is set to 0.65. We use the same value of the constant in our calculations.

The numerical method is second-order accurate in space and time. Similar numerics have been used in detached eddy simulation of supersonic base flows.[2] An implicit full matrix Data-Parallel Lower-Upper Relaxation method[11] is used to integrate the equations in time. The method involves Newton sub-iterations to converge the L_1 norm of the density residual to a prescribed tolerance, taken to be 10^{-6} of a characteristic density in the flow. First order backward Euler time integration is also implemented in the code and is mainly used to integrate through the initial transient flow development.

Grid Design

DES works in the RANS mode in the attached regions of the flow. This includes the forebody and shoulder of the vehicle. Two-dimensional axi-symmetric RANS solutions of the current configuration using the Spalart-Allmaras model are presented in Ref. 12. The salient features of the two-dimensional grids are listed below, and they were used to guide the development of the current three-dimensional volume grids. The outer boundary is carefully tailored such that the grid lines on the forebody are closely aligned with the bow shock wave. A wall-parallel spacing of 1.4×10^{-5}m is required in the nose stagnation region to obtain a grid-independent solution. Along the forebody and shoulder, a wall normal spacing of 1×10^{-5} m is needed to accurately predict the vehicle heating rates, whereas a much coarser grid (5×10^{-5} m) is sufficient on the afterbody.

The baseline volume grid generated for detached eddy simulation is shown in Fig. 2. The multi-block grid has one-to-one grid point matching at the inter-block boundaries. The forebody is spanned by grid blocks I and III. The axi-symmetric grid block III is generated by a revolution of the two-dimensional RANS grid about the vehicle axis. Thus, wall-normal and wall-parallel grid resolution on the forebody and shoulder is maintained to be the same as in Ref. 12 . The azimuthal spacing is dictated by the afterbody grid, as discussed below. In order to avoid grid singularity at the vehicle axis, a non-axisymmetric grid block I is used at the nose. This significantly reduces the grid-sensitivity of the solution in the nose stagnation region. Wall-parallel grid spacing much larger than that in the axi-symmetric simulation could be used. The distribution of points in the wall-normal direction is identical to the RANS grid. On the afterbody, grid blocks II and IV are constructed to allow a careful resolution of the wake, and the region outside the wake is spanned by grid block V. The flow in the outer inviscid region is expected to be relatively steady, axi-symmetric, and similar to the RANS solution. The grid spacing in block V is therefore maintained to be smaller than or comparable to that used in the axi-symmetric simulationThe overall three-dimensional multi-block grid consists of 2.6×10^6 points out of which 9.4×10^5 grid points are concentrated in the focus region.

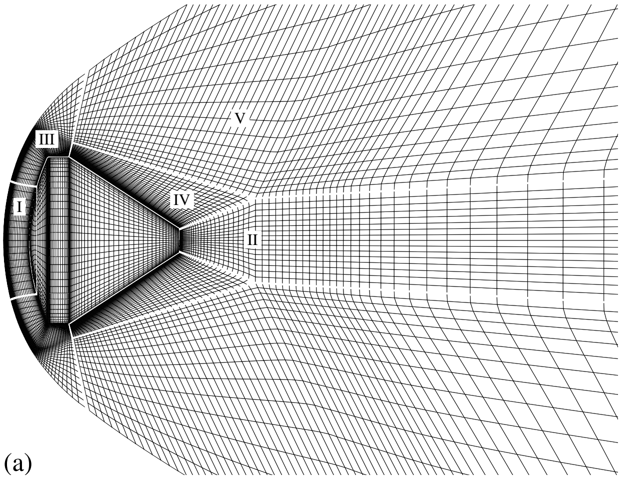

(a)

Figure 2. Three-dimensional grid for detached eddy simulation. Every second point in each direction is shown. White lines denote grid block boundaries, and dashed lines demarcate DES flow regions.

Simulation Results

The instantaneous temperature field in a plane through the vehicle axis (Fig. 3a) is used to identify the salient features of the flow. The bow shock ahead of the vehicle results in high-temperature subsonic flow on the forebody. The Mach number exceeds one just before the first expansion corner. The temperature drops significantly as the gas expands around the vehicle shoulder. The boundary layer that develops on the vehicle becomes turbulent along part of the forebody and on the shoulder. The flow remains attached through the first expansion, but separates immediately downstream of the second corner. The recirculation region extends up to the neck, which is located between 0.7 and 0.8 D downstream of the base. A re-compression shock wave is formed at this location that results in high temperature in the neck region. The wake expands to supersonic Mach numbers downstream of the re-compression shock. By comparison, the recirculating flow is mostly subsonic with small pockets of supersonic flow.

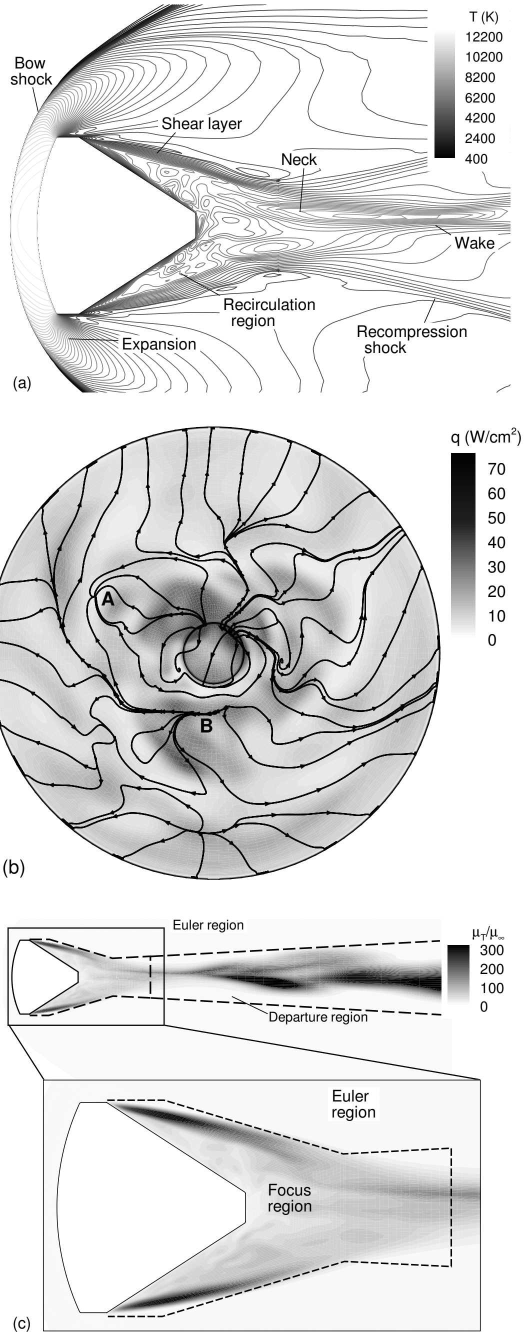

Figure 3. A snapshot of the flow field around the vehicle: (a) temperature contours, (b) surface streamlines on the afterbody, and (c) normalized eddy viscosity distribution. The data corresponds to a single time realization at 264 t_{flow}.

The flow in the recirculation region is highly unsteady and is characterized by vortices and shear layers of varying intensity and length scales. Small vortices (with diameter as low as $0.02D$) are found close to the shear layer and the body surface, whereas large scale motion (about $1.5D$ in size) spans the entire recirculation region. The flow in the recirculation region is also highly three-dimensional, as can be seen from the afterbody surface streamlines plotted in Fig. 3b. The local heat transfer rate to the vehicle is also shown. There is considerable flow in the circumferential direction with several regions of converging and diverging streamlines. The converging streamline patterns correspond to local flow separation and thus a low heat transfer rate to the vehicle wall (for example, at point A). Conversely, local flow reattachment results in a diverging streamline pattern along with high heating rate to the vehicle wall (near point B).

Figure 3c presents the normalized eddy viscosity. The boundaries of the focus, departure, and Euler regions are also shown to verify the grid design methodology. There is very little eddy viscosity in the Euler region, and the flow here is mostly inviscid, steady, and axi-symmetric. In the focus region there is a significant level of eddy viscosity in the shear layer close to the separation point. The shear layer is found to be relatively steady, and axi-symmetric in this region. High aspect ratio cells with large circumferential spacing and fine grid spacing in the axial and radial direction are well-suited for resolving the shear layer. By comparison, the flow in the remaining part of the focus region is unsteady, and has a much lower level of μ_t that supports a range of length scales in this region. In the departure region the axial grid spacing increases downstream of the neck resulting in high eddy viscosity ($\mu_t \propto \Delta^2$) that dissipates the small scale motion. However, large-scale unsteadiness persists in the wake.

The simulation is run until $t = 300\ t_{flow}$ and the time-averaged flowfield is computed over this period. Fig. 4 shows the time-averaged temperature distribution around the vehicle. A few representative streamlines are also plotted. The temperature field outside the wake and on the forebody are similar to the single time realization shown in Fig. 3a. By comparison, the complex recirculating pattern in the instantaneous flow field is replaced by a relatively smooth temperature distribution in the time-averaged data. The time-averaged wake is dominated by a single toroidal vortex that extends to about 0.68 D downstream of the base. The flow is close to being axi-symmetric with very little flow in the circumferential direction.

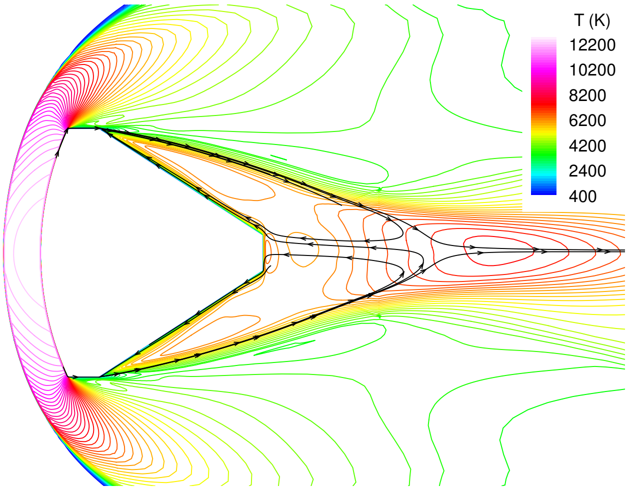

Figure 4. Time-averaged temperature distribution and representative streamlines in the flow around the re-entry vehicle.

Effect of Reynolds Number

A second set of simulations are carried out at a free stream density of 0.082 kg/m^3, which is higher than the earlier value by a factor of 10. The other freestream quantities are maintained at their original value listed earlier. Results are thus compared to the lower density computation to study the effect of Reynolds number on the flow pattern and aerodynamic characteristics. The simulations considered in this section are performed on a finer grid (focus region target grid size is 0.0125 D) than the one described above. The wall normal spacing on the afterbody is decided on the basis of RANS simulations at the two conditions.

Figure 5 compares the afterbody flowfield at the two Reynolds number in terms of the time-averaged density and temperature contours. The density contours match well outside the recirculation region, when normalized by the free-stream density in each case. This includes the shear layer, recompression shock, and neck region. There are differences in the recirculation bubble: ρ/ρ_∞ in the lower Re case $(0.2 - 0.25)$ is higher than that at the higher Re (~ 0.15). Difference also show up near the vehicle wall where the lower Re case has a thicker boundary layer. The time-averaged temperature fields shown in Fig. 5b are significantly different. The shear layer, recirculation bubble, and neck region in the high density simulation are hotter by about 2000 K than the low density case. The gas temperature downstream of neck and in the outer flow are almost identical in the two cases. Higher temperature and lower normalized density in the high Re near wake tend to counteract each other to result in a normalized pressure (p/p_{infty}) that is comparable to the lower Re value. Entire recirculation region and neck is subsonic in both cases and the Mach number is higher along the rear stagnation line in the high Re case owing to higher reversed velocity. This results in higher flow compression near the rear stagnation point leading to higher base pressure. The Mach number in the outer inviscid flow is between 3 and 3.5 in both cases, and the strength of the recompression shock is identical.

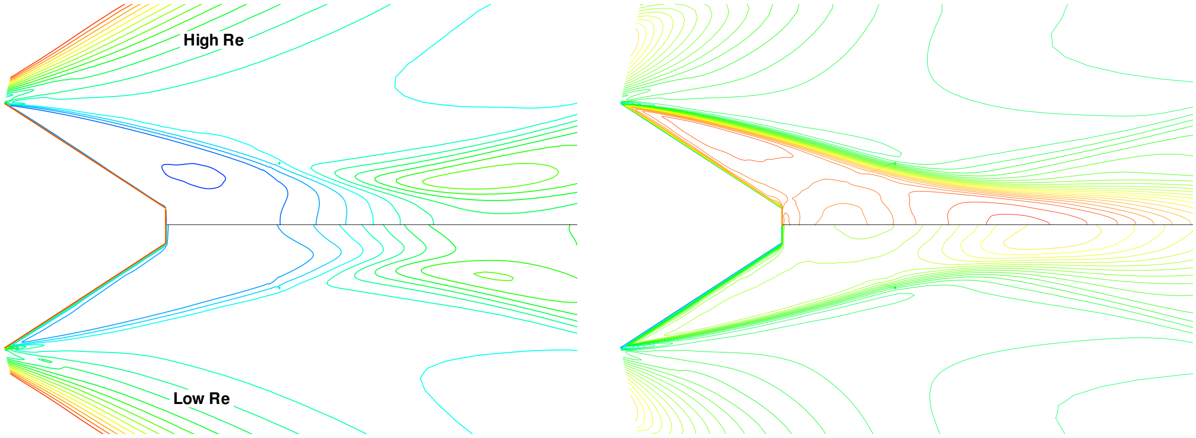

Figure 5. Time-averaged flow pattern computed using DES at two different Reynolds numbers: (a) normalized density contours, (b) Temperature contours.

Figure 6 compares the ratio of eddy viscosity to the local molecular viscosity computed at the two conditions. This ratio gives a measure of the level of turbulence predicted by the model and its effect on the mean flow. At the low Re condition, the entire afterbody and wake flow is predicted to be laminar $(\mu_t/\mu < 1)$ except for the shear layer in the vicinity of the shoulder sepration point. Therefore it is not surprising that the pressure and heat transfer in this DES is close to the laminar results (discussed below). At the higher density μ_t/μ is much larger, reaching up to about 70 in the shear layer and neck region. However, the eddy viscosity level is low $(\mu_t/\mu < 1)$ in the recirculation bubble resulting in laminar flow there. The shear layer location is not affected by the turbulence, but its spreading rate is enhanced compared to the low Re result. Eddy viscosity level increases through the recompression region, reaching maximum value (200μ) behind the neck. Thereafter, ν_t decreases as the wake flow expands and the mean velocity gradients become weaker.

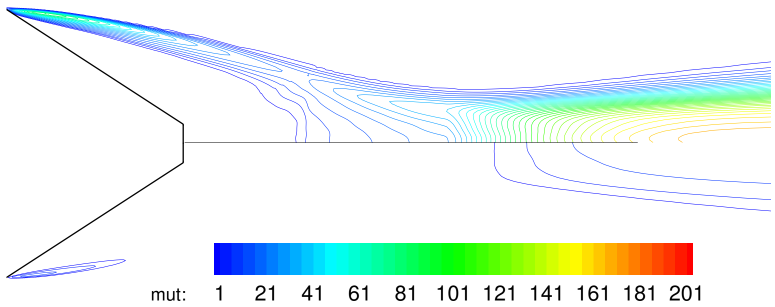

Figure 6. Distribution of eddy viscosity, normalized by the local molecular viscosit, in the time-averaged flow field at two different Reynolds numbers.

The outer flow Mach number in both cases is between 3.0 and 3.5. For these Mach number values, Lees' correlation gives the transition Reynolds number in the range of $1 - 4 \times 10^5$. Reynolds number per unit length along the outer edge of the free shear layer is around 1.4×10^5 and 1×10^6 at the two Re conditions. Thus, in the high Re case the shear layer can transition as early as 0.2 D (running length) from the shoulder, whereas shear layer transition in the low Re case is not until 1.2 D (close to the neck) from the separation point. This trend is captured well in the simulation with DES predicting significant eddy viscosity in the entire shear layer enclosing the separation bubble of the high Re wake. In the low Re case, eddy viscosity levels are negligible until downstream of the neck.

In the recirculation bubble, unit Reynolds number in the higher density case is an order of magnitude larger than in the lower density simulation. This results in a larger range of length scales in the high Re flow, with eddy size as low as 0.12 D near the base, whereas the smallest eddies in the low Re case are about 0.2 D in size. The range of length scales captured in a simulation is determined by the effective viscosity with is a sum of the molecular, numerical and eddy viscosities. The effect of eddy viscosity in the core flow is negligible ($\nu_t/\nu \ll 1$) in both cases. The numerical dissipation is also comparable as identical grid and numerical method are used in the two simulations. Molecular viscosity is about 20% higher in the higher density case owing to higher temperature in this region. The range of time scales in the core flow is found to be similar in the two simulations with smallest time scale around 0.3 t_{flow}.

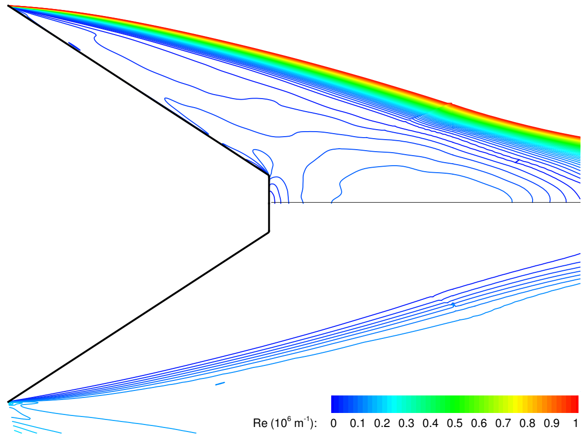

Figure 7. Distribution of local Reynolds number per unit length in the time-averaged flow field at two different Reynolds numbers.

Figure 8 shows the temperature contours in several cross-sectional planes, which span through the recirculation region, reattachment and the wake downstream on the neck. The structure of the shear layer and how the three-dimensional flow develops along the wake are distinctly visible in the figure. The data presented correspond to a single time realization of the flow computed at the lower Reynolds number. The shear layer formed due to boundary layer separation (at $x/D = 0.25$) remains mostly axi-symmetric up to $x/D = 0.60$, while the flow enclosed in the annular region is three-dimensional. As the size of the conical afterbody diminishes, the cross-sectional extent of the recirculation region increases leading to higher level of mixing. There is a low temperature region next to the wall and some of the cold fluid from this region is swept into the core flow of the separation bubble (for example, in the upper left part of $x/D = 0.75$ section).

The shear layer is found to develop instabilities leading to formation of periodic structures along its circumference ($x/D = 0.75 - 1.05$ stations). This is similar to the large-scale turbulent structures experimentally observed in compressible base flows by Bourdon Much like the experiment, about 10-12 structures are found along the shear layer, and their spacing is relatively uniform along the circumference. Examination of several time-realizations of the flow field shows that the number of these turbulent structures at a particular location is in agreement with the experimental results.[13]

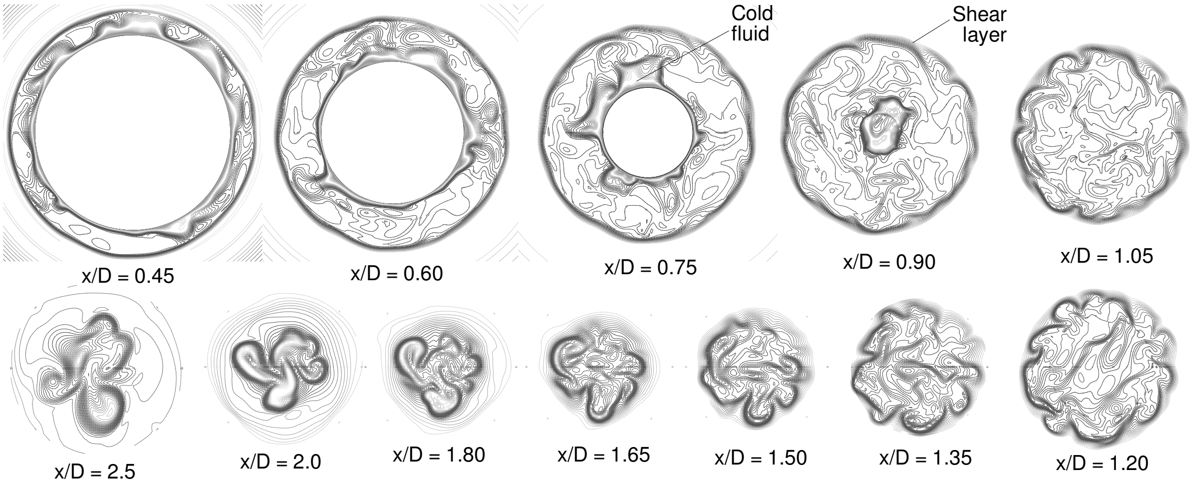

Figure 8. Development of the shear layer enclosing the wake behind the re-entry vehicle at the low Re condition. Temperature contours are plotted in cross-sectional planes through the wake flow.

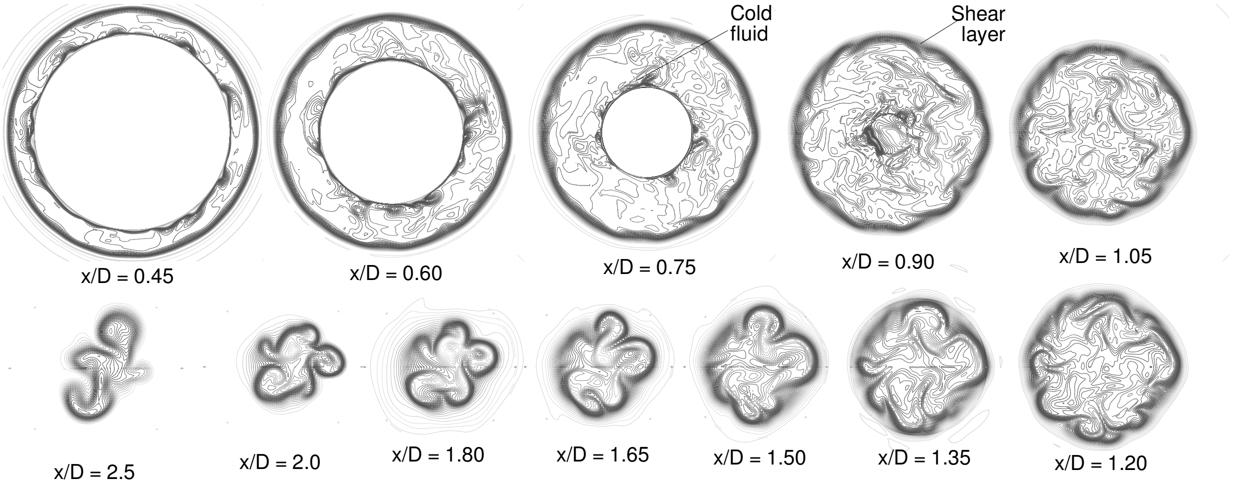

Figure 9. Development of the free shear layer in the high Re simulation at Mach 16. Temperature contours are plotted in cross-sectional planes through the wake flow.

As the wake is compressed in the neck region ($x/D = 1.2 - 1.8$ stations) the shear layer moves closer to the axis and its circumference shrinks. The turbulent structures are found to merge so that their number decreases to about 3-4 in the developing wake ($x/D \geq 2$). Once again, this trend is in close agreement with the experimental observations of Bourdon *et al.*[13] Temperature in wake increases as it is compressed in the neck region, and then decreases as the wake expands downstream.

The results for the higher Re case in Fig. 9 show a very similar trend, although the temperature levels are significantly higher than the data presented above. Higher eddy viscosity in the high Re shear layer makes it thicker. Also, the boundary layer on the vehicle is thinner at higher density and the injection of cold fluid into the core flow is much less prominent. Overall trend of number of lobes and how they develop through the neck compression is akin to the low Re case.

Surface pressure and heat transfer rates for the two simulations are compared in Fig. 10. Pressure normalized by the free-stream pressure is identical in both cases. The stagnation point pressure is 330 p_∞ and it shows the familier parabolic profile on the spherical forebody followed by sharp drop at the expansion corners on the shoulder (at $s = 0.52D$ and 0.64 D). Heat transfer is significantly different in the two cases. Nose stagnation point heating rates are 242 W/cm^2 and 659 W/cm^2 in the low and high Re simulations. For comparison between the two cases, the surface pressure and heating rates are normalized by the respective nose stagnation values. In the low Re case, the boundary layer transitions at $s \sim 0.3D$ and shows only a slight increase in heating rate as compared to the laminar results. This is because of the low eddy viscosity level in the boundary layer. The high Re simulation has a much earlier transition (at $s \sim 0.1D$) and a steeper increase in heating rate. The peak heating at the expansion corner of the high Re flow is about 923 W/cm^2.

Afterbody surface data is shown in Fig. 10b, where the pressure and heat transfer scales are magnified to emphasize the low values on the afterbody. Once again, normalized pressure is identical in the two cases except for a higher value (by 23%) at the base of high Re simulation. This is due to the higher compression observed in this region as compared to the low Re case. Heating rate on the afterbody show similar variatiion at both conditions: increase at separation point followed by decrease on the frustum; there is a broad peak in heating rate near the base-frustum corner with high values at the base. The normalized heating rates (plotted in the figure) for the low Re case are about 50% or lower than the corresponding high Re data. For the high Re condition, the base heating rate is about 22% of the forebody stagnation value, whereas it is less than 10% for the low Re case. The absolute values of heat transfer rate in the two cases differ by a much higher factor. In the higher density case, the heating rate varies between 37 and 171 W/cm^2 on the afterbody, whereas the corresponding numbers for the lower density simulation are 7 and 30 W/cm^2.

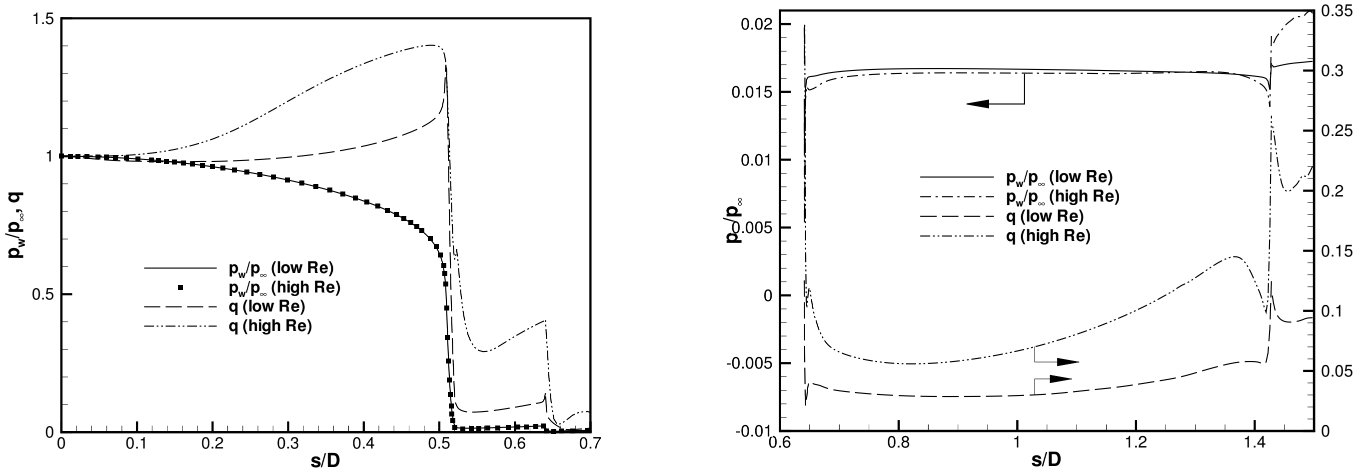

Figure 10. Normalized pressure and heat transfer rate for the two computations: (a) forebody, and (b) afterbody data. The data are normalized by the corresponding nose stagnation values.

Shear layer impingement heating on the afterbody is a major concern in re-entry vehicles. In the current configuration, the free shear layer enclosing the separation bubble does not reattach on the afterbody. Nevertheless, the potential of shear layer impingement is studied in terms of the location and trajectory of the free shear layer. The peak heating at impingement will depend on the maximum gas temperature in the shear layer. Hotter shear layer is expected to give higher peak temperature at the neck stagnation point. The effect of Reynolds number on the location and magnitude of the peak temperature along the rear symmetry line is studied in Fig. 11a. Here, x is measured axially from the vehicle base. RANS results are also included for comparison. In addition, prediction of different simulation methods like DES, axisymmetric RANS, 3D laminar and axisymmetric laminar are compared in Fig. 11b at the lower Reynolds number.

The time-averaged DES flowfield in Fig. 5 shows similar separation bubble size at the two Reynolds numbers. The location and trajectory of the free shear layer, identified in terms of the limiting stream line originating from the shoulder separation point, are also close in the two cases. The resulting neck stagnation point are closely placed with the higher Re solution ($x/D \sim 0.96$) somewhat close to the base than the lower Re case ($x/D \sim 1.2$). Also,the peak temperature in the higher Re flow is about 8400 K, which is higher than the lower Re case by 1700 K. By comparison, the separation bubble computed using RANS are about half the size of the DES results. The location and peak temperature at neck stagnation point in the two RANS solutions show the same with Reynolds number as observed in DES. $(x/D)_{stg}$ is lower by 20% and T_{stg} higher by about 900 K in the higher Re case.

Figure 11b shows the temperature distribution along the vehicle axis downstream of the base as computed by different approaches at the lower Re condition. As mentioned earlier, the wake is expected to transition close to the neck, and DES predicts a laminar core flow and a marginally turbulent shear layer near the shoulder separation location. The resulting effect on the location and magnitude of peak temperauture at neck is minimal, with the DES results matching 3D laminar computation ($\nu_t = 0$) closely. Once again, RANS simulation yields a much smaller and hotter wake. T_{stg} is about 2300 K higher than DES. By comparison, results from an axisymmetric laminar flow simulation at identical conditions are comparable to the three-dimensional laminar and DES computations. The main differences being in the lower peak temperature at neck and the presence of a base shock at 0.1 D downstream of base. Note that the axisymmetric laminar simulations result in multiple unsteady vortices in the recirculation bubble.

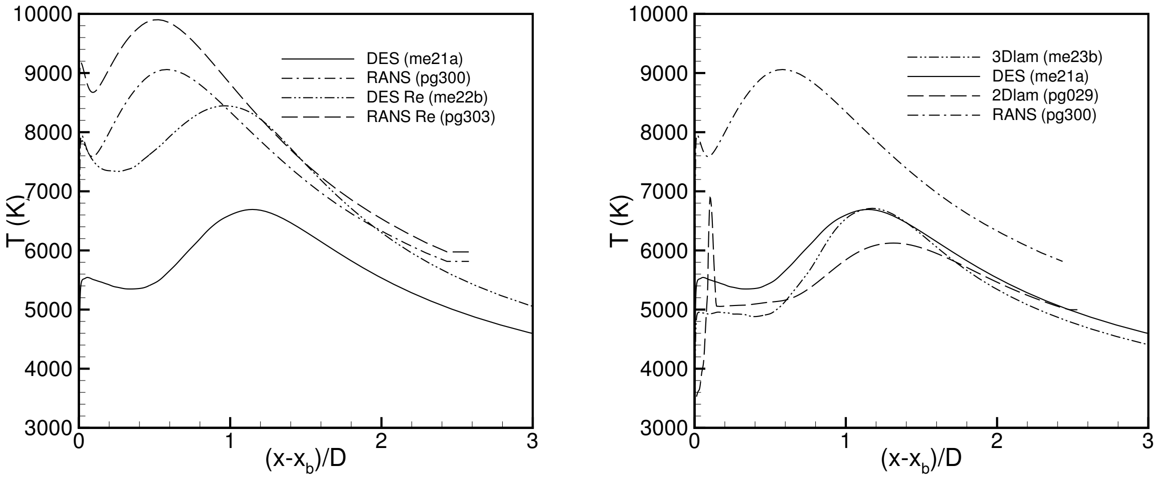

Figure 11. Temperature distribution in the axial direction downstream of the vehicle base: (a) RANS and DES results at two different Reynolds numbers, and (b) results obtained by different simulation approaches at the lower Re condition.

Conclusions

The present work employs detached eddy simulation to study the hypersonic base flow for a capsule re-entry configuration. Multi-block finite-volume grids are generated to resolve the strong shocks and expansions typical of hypersonic blunt body flows, and to meet the requirements of detached eddy simulation in the wake. The flow on the afterbody is highly three-dimensional and unsteady, and the shear layer is found to develop periodic circumferential structures. The number and topology of these structures closely match those seen in experiments of supersonic base flows. Time-averaging yields almost uniform pressure along the frustum and higher value in the base stagnation region. The afterbody heat transfer rate of these low *Re* flows is mostly determined by the LES part of the simulation, and not by the RANS model effective in the near-wall region. It is also found to be relatively insensitive to variations in the RANS/LES transition location. Grid refinement in the DES focus region results in lower eddy viscosity which in turn leads to a larger recirculation zone, higher pressure and lower heating rate on the afterbody. The fine grid results are found to be close to the fine-grid laminar solution, with vanishing eddy viscosity. Thus, unlike fully turbulent flows, DES of this low *Re* hypersonic configuration approaches direct simulation of the flow. Control of the numerical dissipation is therefore essential to obtain a grid-converged solution. On the whole, the current work is a careful application of DES to a low Reynolds number and high Mach number re-entry configuration. It gives valuable insights into the flow physics and the numerical and modeling issues involved in the DES methodology.

References

[1] Wright, M.J., Brown, J.L., Sinha, K., Candler, G.V., Milos, F.S., Prabhu, D.K. "Validation of Afterbody Aeroheating Predictions for Planetary Probes: Status and Future Work". *2nd International Planetary Probe Workshop*, 2004.

[2] Forsythe, J.R., Hoffmann, K.A., and Squires, K.D. "Detached-Eddy Simulation with Compressibility Corrections Applied to a Supersonic Axisymmetric Base Flow". *AIAA Paper*, 2002-0586, 2002.

[3] Sinha, K., Barnhardt, M., and Candler, G.V. "Detached Eddy Simulation of Hypersonic Base Flows with Application to Fire II Experiments". *AIAA Paper*, 2004-2633, 2004.

[4] Barnhardt, M., and Candler, G.V. "Detached Eddy Simulation of Hypersonic Base Flows During Atmospheric Entry". *AIAA Paper*, 2006-3575, 2006.

[5] Slucomb, T.H. "Project Fire II afterbody Temperatures and Pressures at 11.35 Kilometers per Second". *NASA TM X-1319*, 1966.

[6] Lees, L. "Hypersonic Wakes and Trails". *AIAA Journal*, 2(3), 1964.

[7] MacCormack R.W. and Candler G.V. "The Solution of the Navier-Stokes Equations Using Gauss-Siedel Line Relaxation". *Computers and Fluids*, Vol. 17, No. 1, pp. 135-150, 1989.

[8] Sinha K. and Candler G.V. Convergence improvement of two-equation turbulence model calculations. *AIAA Paper*, 98-2649, 1998.

[9] Sinha K. Olejniczak J. Candler G. V. Magruder T.D. Wright, M.J. and A.J. Smits. "Numerical and Experimental Investigation of Double-cone Shock Interactions". *AIAA Journal*, 38(12), 2000.

[10] Shur. M., Spalart, P.R., Strelets, M., and Travin, A. "Detached Eddy Simulation of an Airfoil at High Angle of Attack". *4th Int. Symp. Eng. Turb. Modelling and Measurements, Corsica*, 1999.

[11] M.J. Wright, G.V. Candler, and M. Prampolini. "Data-Parallel Lower-Upper Relaxation Method for the Navier-Stokes Equations". *AIAA Journal*, 34(7):1371–1377, 1996.

[12] Sinha, K. "RANS simulation of Fire II re-entry configuration". *International Symposium on Shock Waves*, 2005.

[13] Bourdon, C.J., and Smith, K.M., and Dutton, J.C., and Mathur, T. Planar visualization of large scale turbulent structures in axisymmetric supersonic base flows. *AIAA Paper*, 98-0624, 1998.